

Full length article

Optical sensor arrays designed for guided manufacture of perfluorocarbon nanoemulsions with a non-synthetic stabilizer



Ryan Bardsley^b, Graeme Gardner^a, Hubert M. Tse^c, Christopher A. Fraker^{a,*}

^a Diabetes Research Institute, University of Miami Miller School of Medicine, Miami, FL 33136, USA

^b Design for Complex Systems, Inc. 1 Burnham Ln, Manchester, MA 01944, USA

^c Department of Microbiology, The University of Alabama at Birmingham, Birmingham, AL 35294, USA

ARTICLE INFO

Article history:

Received 25 June 2021

Revised 16 September 2021

Accepted 20 September 2021

Available online 24 September 2021

Keywords:

Nanoemulsions

Microfluidization

Surfactant

Perfluorocarbon

Drug development

Tissue engineering

Encapsulation

ABSTRACT

Hydrophobic drugs are incorporated into oil-in-water nanoemulsions (OIW) either as new formulations or repurposed for intravenous delivery. Typically, these are manufactured through stepwise processes of sonication or high-pressure homogenization (HPH). The guiding criteria for most nanoemulsion manufacture are the size and homogeneity/polydispersity of the drug-laden particles with strict requirements for clinical injectables. To date, most formulation optimization is done through trial and error with stepwise sampling during processing utilizing dynamic light scattering (DLS), light obscuration sensing (LOS) or laser particle tracking (LPT) to assess manufacturing progress. The objective of this work was to develop and implement an in-line optical turbidity/nephelometry sensor array for the longitudinal in-process monitoring of nanoemulsion manufacture. A further objective was the use of this sensor array to rapidly optimize the manufacture of a sub-120 nm oxygen carrying perfluorocarbon nanoemulsion with a non-synthetic stabilizer. During processing, samples were taken for particle size measurement and further characterization. There was a significant correlation and agreement between particle size and sensor signal as well as improved process reproducibility through sensor-guided manufacture. Given the cost associated with nanoemulsion development and scale-up manufacture, our sensor arrays could be an invaluable tool for efficient and cost-effective drug development. Sensor-guided manufacturing was used to optimize oxygen-carrying nanoemulsions. These were tested, *in vitro*, for their ability to improve the viability of encapsulated endocrine clusters (mouse insulinoma, Min6) and to eliminate hypoxia due to oxygen mass transfer limitations. The nanoemulsions significantly improved encapsulated cluster viability and reduced hypoxia within the microcapsule environment.

Statement of significance

Nanoemulsions are rapidly becoming vehicles for the controlled release delivery of both hydrophilic and hydrophobic drugs given their large surface area for exchange. As work shifts from bench to large scale manufacturing, there is a critical need for technologies that can monitor and accumulate data during processing, particularly regarding the endpoint criteria of particle size and stability. To date, no such technology has been implemented in nanoemulsion manufacture. In this paper we develop and implement an optical sensor array for in-line nanoemulsion process monitoring and then use the array to optimize the development and manufacture of novel reproducible oxygen carrying nanoemulsions lacking synthetic surfactants.

© 2021 The Authors. Published by Elsevier Ltd on behalf of Acta Materialia Inc.
This is an open access article under the CC BY-NC-ND license
(<http://creativecommons.org/licenses/by-nc-nd/4.0/>)

1. Introduction

With advances in microfluidization and high pressure/high shear processing, there has been a recent growth in the development and optimization of clinically relevant nanoemulsions for the delivery of therapeutic pharmaceuticals and nutraceuticals [1–7].

* Corresponding author.

E-mail address: cfraker@med.miami.edu (C.A. Fraker).

The use of oil-in-water (OIW) formulations to deliver or repurpose hydrophobic drugs is one area where both academic and industry researchers have expanded efforts to harness emulsion nanoparticles for rapid and homogenous delivery through topical, oral and intravenous routes [5,8–15].

Typically, OIW nanoemulsions are comprised of a hydrophobic/apolar core region, also called the internal or discontinuous phase which serves as a carrier for the hydrophobic active compound. This portion is mixed with an emulsifying agent/surfactant which serves as an intermediate phase stabilizing the emulsion nanoparticles. The final phase is the continuous or aqueous phase, where the nanoparticles are dispersed. The advantages of nanoemulsions for the delivery of active compounds are the small particle size and homogeneity of the mixtures which leads to an increased surface area for delivery and overall higher bioavailability.

One example of well-studied OIW nanoemulsion formulations are those manufactured using perfluorocarbon (PFC) carriers for numerous pre-clinical and clinical applications including artificial blood, diagnostic imaging, organ preservation and intravenous delivery of anesthetics and other pharmaceutical agents [8–10, 16–23]. Formulations for PFC nanoemulsions include lipids, phospholipids and numerous surfactants, generally from the polyethylene glycol (PEG) amphiphilic di-block copolymer family, as the intermediate phase. The continuous phase is comprised of physiological buffer solutions and for the discontinuous phase, numerous PFCs have been utilized, either with or without hydrophobic active agents. With the advances in processing and characterization equipment, groups, including our own, can achieve the sub 200 nm particle size needed to prevent immune activation observed in prior preparations [10,24–31].

The manufacture of nanoemulsions is usually a two-step process of pre-emulsification involving high-shear mixing using a rotor-stator or sonication followed by high-pressure homogenization (HPH). HPH is performed passing mixtures through specially designed interaction chambers under conditions of high pressure/high shear that results in the rapid generation of sub-micron particles. The longitudinal stability of the final nanoemulsions is critical to the utility of the formulations as particle size growth can affect the safety of preparations when used intravenously as an example [10,25].

Historically, most nanoemulsion manufacture has relied on random sampling or end-point measurements of particle size using methods such as dynamic light scattering (DLS), light obscuration or more recently, nanoparticle tracking systems (NPT) and tunable resistive pulse sensing (TRPS). Characteristic of most nanoemulsions is a concomitant increase in transmittance/decrease in absorbance associated with a decrease in mean particle size. These measurements are used to inform changes in manufacturing protocol based on desired endpoint related to particle size but due to their infrequency fail to capture critical information about the longitudinal processing. Variables such as temperature, pressure and processing time also can have an effect on particle size. There have been sporadic research efforts with optical probes inserted into manufactured nanoemulsions to study, primarily, emulsion aging. In one study, these sensor probes were used to send signals to modular UV/Vis spectrometers for spectral analysis at multiple wavelengths at fixed and relatively time gaps [32]. To our knowledge, however, no one has utilized sensors in the fluid path during processing in short time scales. Given the increased interest in formulation/reformulation of drugs into nanoemulsions, there is a critical need for instrumentation that can guide processing in real-time thereby reducing costly mistakes in both small-scale and large batch manufacturing.

Optical sensors, more specifically turbidity sensors, have long been used in flow-based measurements as they measure the

amount of light scattered by “solid” objects in a fluid as it crosses an optical path. Marrying this concept to microfluidic nanoemulsion processing to measure discrete changes in formulation processing seemed a logical step to more informed manufacturing. In this work, we developed perfluorocarbon nanoemulsions of sub 120 nm particle size using bovine serum albumin as the intermediate phase. We hypothesized that the development of an in-line optical turbidity/nephelometry sensor array for continuous monitoring of nanoemulsion processing would allow for a rapid acquisition of optimal microfluidization settings and reproducibility. The goal of the work was to determine if we could consistently produce nanoemulsions using the same materials and processing for a fixed time. We followed the optical signal to determine if process completion and particle size coincided with a signature hypothesized to be a region of minimal signal change (plateau) in the nephelometry signal. Additionally, we hypothesized that data collected from the optical sensor array could be correlated to DLS particle size measurements and used to derive a real-time predictor of particle size during specific nanoemulsion manufacture. The benefits of these sensor arrays would be reductions in time and cost related to the development of pharmaceutical and nutraceutical nanoemulsion formulations. As an example, we manufactured perfluorocarbon nanoemulsions utilizing bovine serum albumin as a stabilizer to generate sub 120 nm biocompatible drug/oxygen carriers and tested the oxygen carrying capacity/effect on encapsulated 3D cell cluster viability. While albumin has been utilized as an emulsifier in prior works, most have described emulsions having characteristic particle sizes ranging from 140 nm to greater than 500 nm, typically classified as microemulsions given the sub-120 nm particle size criteria generally used to classify nanoemulsions [33–37].

2. Materials and methods

2.1. Optical turbidity/nephelometry sensor design

Turbidity is typically used as a measure of the degree of transparency of water/salt solution due to the presence of suspended particles. The greater the amount of suspended particles in the water/salt solution, the less light passes through it and the higher the turbidity. While many techniques for measuring turbidity of a solution have been developed, the underlying premise involves a light source aimed at a fluid channel. The light which passes through the channel is scattered by the particles suspended in the fluid. A series of light detectors arranged around the fluid channel measures light that is transmitted through, reflected back, or scattered at specific angles. There are many international standard methods for measuring these qualities accurately (ISO 7027, EPA 180.1, Hach 10133).

As this sensor was originally designed to quantify particle size in a nanoemulsion of saline, intermediate phase/nanoemulsion stabilizer and perfluorocarbons, turbidity as a concept for measurement was still appropriate. However, the positive and negative associations of murky, highly-turbid water being of poor quality and clear, low-turbidity water being of good quality were disregarded in this application. The described methodology used the amount of scattered and transmitted light measured to follow the decrease in average particle size of the fluid passing through the sensor throughout the manufacturing process. It did this accurately and in real-time: an important feature in short-run, small-volume pharmaceutical research and manufacturing processes.

The sensing device utilized a single infrared light emitting diode (IR LED) with a peak wavelength λ of 940 nm. This is different from the prior probe sensors coupled with modular UV/Vis spectrometers mentioned, above, which measure multiple wavelengths at fixed increments giving complete spectral shifts as opposed to changes in single wavelengths [32]. An ON Semiconduc-

tor QEE113 High Power Infrared Emitter was selected with a radiant intensity of 12 mW/sr, increasing its chances of light passing through opaque liquids to fall on the photosensors. The QEE113 LED was a gallium arsenide (GaAs) sidelooker package with a medium wide emission angle of 50 °. Peak radiation vectors at approximately 75 ° and 105 ° normal to the lens were used to align the incident and transmitted light sensors. The GaAs-based LED was specifically selected due to its insensitivity to overheating and reduced noise emission. Its rise and fall times of 800 ns were accounted for in the speed of the sensing subroutine.

Aligned to the IR LED's optical plane, were three optical light-to-voltage (LTV) sensors with a fourth light-to-voltage sensor oriented orthogonally at 90 ° to the optical axis to form the nephelometric optical path. The sensors used were four TAOS monolithic silicon photodiodes with integrated transimpedance amplifiers. Their output voltage was directly proportional to the light intensity (irradiance) received by the photodiode. These devices have improved amplifier offset-voltage stability and are supplied in a 3-lead clear plastic sidelooker package with an integral lens.

The IR signal was regulated by a 16-bit pulse-with-modulation (PWM) controller that adjusts frequency to maintain a constant intensity regardless of temperature or LED age. The first light to voltage sensor was pointed directly at the LED positioned before light passes through the fluid sensor and was read by a 12-bit analog to digital converter (ADC). Additional light passed directly through the fluid channel where the nanoemulsion travelled during processing and an IR light to voltage sensor aligned with the LED read absorbance through another 12-bit ADC. Another sensor was positioned perpendicular to the fluid channel and collected the nephelometry signal through another 12-bit ADC. Finally, backscatter signal was collected through another LTV sensor positioned 135 ° relative to the light source. Each ADC was then read using differential measurements. To each input, a 12-bit digital to analog converter (DAC) was connected and tuned to provide a maximum output over typical irradiances using standards in compliance with the ISO 7027 guidelines (Formazin standards). Data output from the sensor array was collected in real-time at a frequency of 0.5 Hz using a serial data communications package, in this case the macOS Terminal emulator. Data collected from the sensor array included arbitrary units of intensity and voltages along with unit temperature and a time stamp.

2.2. Sensor array calibration/optimization

Prior to implementation in the nanoemulsion processing, the sensor array was calibrated and tested to maximize signal output range and sensitivity. Irradiance levels were first measured with all light sources off and dark adjustment within the unit housing to determine the “dark” values for all light to voltage sensors at all gain settings. Next a sequence of gradual IR sensor intensity increases was performed at all gain settings with corresponding measurements. This was performed for the entire 16-bit range of the TSL7611 sensors. Using the measurements, the range between the dark voltage readings for each sensor at each gain setting and the LED intensity value which yielded the maximum irradiance for the sensor was determined. These settings were implemented during each sensing loop. Prior to each use of the sensor, the unit was programmed to run a self-check script to insure maximal sensor output.

2.3. Nanoemulsion materials

Bovine serum albumin (BSA) was purchased from VWR. Perfluorotributylamine (FC-43) was purchased from 3 M. Phosphate buffered saline (PBS), pH 7.2 without Ca^{2+} , Mg^{2+} was purchased from Thermo Fisher Scientific (0.9 g/L sodium chloride, 0.21 g/L

potassium phosphate monobasic and 0.726 g/L sodium phosphate monobasic; 280–320 mOsm).

2.4. Nanoemulsion premix manufacture

BSA was dissolved at a concentration of 100 mg/mL in PBS overnight at room temperature with stirring (10% w/v stock). In an 80 mL beaker, a concentrated premix was made with 37.5 mL of 10% w/v BSA stock and 7.5 mL of perfluorotributylamine (FC-43). The 7.5 mL of FC-43 was added in a step-wise fashion to the BSA while using an IKA Ultra-Turrax® T25 dispersing instrument fitted with an S25N-10G dispersing element at 7,500 rpm to homogenize the premix for 5 min. The final relative concentrations of the premix ingredients were 8.33% w/v BSA and 16.67% v/v FC-43.

2.5. Nanoemulsion microfluidization and optical sensing

Prior to the microfluidization process, the optical sensing and data collection was initiated on the macOS Terminal emulator with PBS representing maximal intensity and minimal absorbance. After 5 min, microfluidization of nanoemulsion premix was performed on a high-pressure/high-shear homogenizer, the ShearJet HL60 from DyHydromatics (Maynard, MA, USA), fitted with a 75.1 T diamond interaction chamber at 30K PSI. Processing temperature was maintained at 4 °C using a recirculating chiller (Polyscience, ¼ HP). The 45 mL premix was recirculated through the optical sensing unit at 60 Hz for a total processing time of 30 min (~13.3 discrete passes). At $T = 0.5, 1, 1.5, 2$ and approximately every 2 min following during processing, 200 μL samples of the recirculating nanoemulsion concentrate were collected for particle size analysis. At the end of the ~30 min processing period, 30 mL of the concentrate was collected. The concentrate was diluted with PBS -/– to 50 mL for a final BSA concentration of 5% w/v and a final FC-43 concentration of 10% v/v. A sample of the diluted nanoemulsion was collected for analysis and then the final product was sterile filtered through a 0.2 μm nylon filter (Pall). A sample of the filtered product was also collected for analysis.

2.6. Particle sizing analysis by dynamic light scattering (DLS) and nanoemulsion stability

The nanoemulsion particle sizes during processing were characterized by dynamic light scattering (DLS) experiments performed on a Malvern Zetasizer Nano ZS with a non-invasive back scatter configuration at 13 + 173 °. The diluent used was PBS -/– and a viscosity of 1 cP at $T = 298$ K was implemented. To optimize measurements and study the effect of dilution on particle stability, measurements were also performed on undiluted and final samples at specific dilutions (10, 25, 50, 150, 500, 750, 1000, 1500x). Measurements were performed on each sample in triplicate with 10 reads per replicate run. Nanoemulsion longitudinal stability was evaluated in a subset of 8 of the 9 successful nanoemulsion manufacturing runs. Samples were taken at day 3–5 and day 14 post-manufacture to determine particle size changes, if any. In our prior works utilizing Pluronic di-block copolymer surfactants, if no change in particle size was observed within 2 to 4 days, long term stability was achieved.

2.7. Perfluorocarbon quantification by attenuated total reflectance Fourier transform infrared spectroscopy (ATR-FTIR)

Nanoemulsion perfluorocarbon content was quantified using attenuated total reflectance Fourier transform infrared spectroscopy (Perkin Elmer Spectrum 100) as previously described with some modifications [10,25]. Briefly, a spectral region unique to perfluorotributylamine (FC-43) was observed in the wavenumber region

from 1080–1380 cm⁻¹. Pure FC-43 and 5% w/v BSA solution were used as standards (100% and 0% FC-43, respectively). Area under the curve between 1080 and 1380 cm⁻¹ and with a horizontal baseline at 1380 cm⁻¹ was calculated for the spectra using the Perkin Elmer Spectrum software. Unknown values were determined using the linear regression of the two-point standard curve. For each standard or sample, a blank was run followed by three measurements of 8 scans with a resolution of 4 cm⁻¹. PFC content in all nanoemulsion concentrates and final diluted preparations was measured.

2.8. Effective oxygen diffusivity and mass transfer enhancement in PFC nanoemulsions

Effective diffusivity of oxygen through nanoemulsion preparations was measured as previously described [25]. Calibrated 5 mm diameter oxygen spot sensors (PreSens GmbH, Regensburg Germany) affixed to the basal surface in 12 well plates were used for longitudinal oxygen measurements in solutions (~2 mm liquid height). 12 well plates were placed in a standard 37°C RA/5% CO² humidified incubator. Oxygen was purged to a final concentration of 5% (~32–34 mmHg) by injecting pure nitrogen. One sensor was designated to monitor chamber environment and the others were utilized for oxygen measurement in solutions. In every experiment, several wells were utilized for base solution (surfactant at 2% w/v concentration) or physiological salt solution controls to ensure sensor accuracy. At equilibrium, sensor logging was initiated and the chamber door was opened to allow influx of air containing oxygen. When the chamber sensor reached room air concentration (~142–145 mmHg), the door was closed. Oxygen partial pressure in the solutions was then measured (2 sec/data point) until equilibration with room air. Liquid volumes were recorded to document evaporative loss, if any.

Diffusion was modeled as that through a single surface of a slab of a given height (in this case, solution volume divided by well surface area). Transient solutions of concentrations were generated by iterative numeration. The diffusion coefficient was determined using least squares curve fitting of measured oxygen concentration to the theoretical model [38]:

$$C = C_s + \frac{4}{\pi} (C_0 - C_s) \sum_{n=0}^{\infty} \frac{(-1)^n}{2n+1} \cos\left[\frac{(2n+1)\pi z}{2a}\right] \exp\left[\frac{-D(2n+1)^2\pi^2 t}{4a^2}\right] \quad (1)$$

Here, C is the concentration at time, t, C_s the max pO₂ measured, C₀ the starting pO₂ measured, z is the height of the sensor above the dish bottom, 50 μm, a is the liquid height, D is the effective diffusivity guess varied to obtain least squares fitting and n is the number of iterations used in the series (n=20). The boundary conditions utilized were the C_s value, assumed to remain constant at the upper nanoemulsion surface, and the assumption of zero flux at the basal well surface. Emulsion base solutions and PBS –/- were used as controls to test the accuracy of the system based on published literature values. For 8 of the 9 nanoemulsion samples and relevant controls, n = 5 technical replicates were performed per experiment.

The solubility of oxygen in perfluorocarbons is reported in the literature to be 20 to 25 times that of aqueous buffer solutions [24, 25, 39]. Utilizing the reported Bunsen coefficients in buffer solutions and perfluorocarbons, the diffusive permeability coefficient expressed in mol/cm/mmHg/s for 8 of the 9 nanoemulsion preparations and the base solution control was calculated using the following equation:

$$P_D = \alpha \cdot D_{eff} \quad (2)$$

where α is the Bunsen oxygen solubility coefficient expressed in mol/mmHg/cm³ and D_{eff}, the measured effective oxygen diffusivity expressed in cm²/s. The calculated values from 8 of the 9 nanoemulsion preparations were used to estimate oxygen mass transfer benefit to 3D endocrine cell clusters encapsulated in alginate hydrogels.

2.9. Optical sensor signal analysis

Comma separated value data (CSV) was captured in the screen-log.csv file generated by the macOS Terminal Emulator. The data was imported, analyzed and graphed in Microsoft Excel for Macintosh (v 16.48) or GraphPad Prism 9 for Mac (GraphPad Software, San Diego, California USA, www.graphpad.com). Longitudinal plots of signal from the turbidity (absorbance) and nephelometry sensor along with reference plots of the intensity and incident light as indicators of temperature effects and compensatory shifts were generated.

2.10. Derivation of formula for particle size prediction

Measured particle sizes were plotted against averaged turbidity and nephelometry signals (10 points around time of each sampling). Non-linear least squares regression analysis was performed to derive a formula for particle size determination from averaged sensor signals.

2.11. Correlation analysis of measured and estimated particle size

Using particle sizes determined from non-linear regression (2.8), correlation analysis was performed on measured particle size relative to calculated particle size. Normality/log normality tests (Anderson-Darling, D'Agostino & Pearson, Shapiro-Wilk and Kolmogorov-Smirnov) were performed to determine data distribution and then the appropriate (Gaussian/Non-Gaussian) correlation test was performed.

2.12. Bland-Altman analysis of measured and estimated particle size

As the measured and predicted particle size were expected to quantify the same construct, assessment of the agreement between the two variables was performed using the Bland-Altman test. A Bland-Altman plot was generated for the data set to determine measurement bias, if any, allowing 5% of the data points falling outside of the upper and lower limits of agreement as an acceptable cutoff *a priori*.

2.13. MIN-6 culture and 3D cluster formation

Murine insulinoma cells (p.30 – 35) were grown in 2D culture using Dulbecco's Modified Eagles Medium (DMEM) high glucose with Glutamax (Thermo Fisher) (400 mg/dL) supplemented with 25 mM Hepes and 1% penicillin and streptomycin. At approximately 75% confluence, cells were removed from culture surface using 1X Trypsin-EDTA solution (0.05% trypsin, 0.02% EDTA, Thermo Fisher), counted using a hemocytometer and resuspended in fresh medium at a density of 1 × 10⁶ cells per mL. Thirty million cells were transferred to a small volume (ABLE bioreactor, 30 mL flask from Reprocell) in 30 mL of medium and stirred at a rate of 60 rpm for 48 h. At the end of the 48 hour period, 3D clusters were counted on an automated 3D aggregate (islet) counter (Biorep, Inc). These clusters were utilized for baseline oxygen consumption measurements for finite element modeling (FEM), baseline viability measurements and for encapsulation in alginate polymer solutions with and without PFC nanoemulsions.

2.14. Oxygen consumption measurements and finite element modeling (FEM)

Baseline oxygen consumption measurements and DNA quantification were performed ($n = 4$ experimental replicates, 4 technical replicates per experiment) on MIN-6 clusters as previously described [40–43]. The calculated oxygen consumption per unit tissue volume was calculated for each technical replicate and averaged amongst all experimental runs to get a mean value for use in FEM.

To assess the oxygen profiles within 1mm microcapsules containing standard volume loading density (1.5% v/v), 2D FEM was performed using Comsol 5.3a based on previous modeling assumptions and constraints [40,44–46]. Tissue oxygen profiles and anoxic tissue volumes ($pO_2 < 0.1$ mmHg) were estimated using volume integrals of the modeled tissue. Volume profiles from control and PFC nanoemulsion configurations were compared to viability measures.

2.15. Polymer preparation and measurement of rheology and osmolarity

Alginate solutions were prepared for use in encapsulation at a concentration of 1.6% w/v by dissolving 16 mg/mL of Ultra Pure Medium Viscosity Gyluronic alginate powder from DuPont Medical (Novamatrix) in either sterile PBS -/- or perfluorocarbon nanoemulsion. The solutions were stirred overnight to fully solubilize the alginate and then were sterile filtered through a 0.2 μ m syringe filter.

The osmolarity of the polymer solutions was determined using the ELITech Vapro Vapor Pressure Osmometer. Briefly, after three-point calibration (100, 300 and 1000 mOsm), samples of both polymer solutions were run in triplicate. As an additional control, PBS -/- was run in triplicate against the certificate of authenticity values.

Flow curves and viscosity curves were generated for each polymer formulation using the Haake RheoStress 6000 fitted with a 35mm spinning plate disc probe to measure shear stress (flow curve) and dynamic viscosity (viscosity curve) across a range of shear rates (through 1000 1/s). The expectation was that both alginate formulations would display typical shear thinning behaviors characteristic of alginate solutions.

2.16. MIN-6 cluster encapsulation

MIN-6 clusters ($n = 3$ experimental runs) were encapsulated in 1.6% UP-MVG alginate made with PBS -/- or PFC nanoemulsion using a parallel air flow droplet generator (Biorep). Solution osmolarity was tested before encapsulation and plate/plate flow rheometry was performed to insure polymer solution consistency amongst the two groups. Briefly, MIN-6 clusters were resuspended in alginate solutions at a density of 8,500 equivalent clusters per mL of polymer. One equivalent is a cluster with a diameter of 150 μ m based on count standardization of islets of Langerhans. Air flow was maintained at 2 L/min and polymer flow at 300 μ L per minute delivered by syringe using a Harvard Apparatus Pump 11 Pico Plus Elite. Droplets were collected in a gelation bath of 50 mM calcium chloride solution adjusted to 300 mOsm with MOPS and D-Mannitol and buffered to pH 7.4 prior to use. The ~1 mm capsules were allowed to gelate for 10 min and were then washed twice with Hanks Balanced Salt Solution containing calcium and magnesium. Finally, the capsules were suspended in DMEM complete culture medium and transferred to 6 well plates for culture at a density of ~1,700 equivalents per well in 2 mL of medium. Culture was carried out for 96 h in a standard 37C RA/5% CO₂ incubator.

On the day of encapsulation, 10 photomicrographs were taken per capsule group and both diameter and volume were quantified.

2.17. Live/Dead Viability Assessment

On day 2 and day 4 post-encapsulation, MIN-6 cluster viability was assessed ($n = 3$ experimental replicates, $n = 6$ technical replicates per time point per group) using the MultiTox-Fluor Cytotoxicity Assay (Promega). In this assay, viability is expressed as the ratio of fluorescence from a live cell dye that becomes inactive with cell permeability and another cell impermeant dye that reacts with a protease released when cells are lysed. This ratio-metric read-out eliminates the need for normalization using DNA or total protein. As controls, cell-free capsules and cell containing capsules incubated with lysis buffer (T-per, Thermo Fisher) were run in parallel. Capsules were incubated for 3 hours with assay solutions and then quantitative fluorescence signal was acquired and analyzed per manufacturer protocol.

2.18. Imaging of tissue hypoxia

To visualize the presence of tissue oxygen profiles $< 38\text{--}40$ mmHg (~5%), Image-IT™ Green Hypoxia Reagent (Thermo Fisher) was used along with LIVE/DEAD™ Fixable Red Dead Cell Stain Kit (Thermo Fisher) and Hoechst 33342 (Thermo Fisher), for nuclear staining. Briefly, 50 capsules per group were plated in a 6-well plate with 1.5 mL of complete culture medium supplemented with 10 μ L Image-IT™ Green Hypoxia Reagent, 1:1000 dilution (1.5 μ L) of LIVE/DEAD™ Fixable Red Dead Cell Stain and 20 μ m Hoechst 33342 (1:1000 dilution of 20 mm stock). Capsules were incubated for 6 hours in a 37C RA/5% CO₂ incubator. At the end of the incubation period, the capsules were washed three times with HBSS +/+ and imaged

2.19. Statistical Analysis

Unless otherwise stated, all data is expressed as the mean \pm SD. For all statistical analyses, GraphPad Prism 9 for Mac (GraphPad Software, San Diego, California USA, www.graphpad.com) was utilized. Normality was tested using four conventional methods provided in the software package (Anderson-Darling test, D'Agostino & Pearson test, Shapiro Wilk test and the Kolmogorov-Smirnov test). Depending on normality, either ANOVA or the non-parametric Kruskal-Wallis test was utilized for comparison amongst the control and nanoemulsion encapsulation groups. A p-value of 0.05 or lower was considered significant for observed differences between the two groups.

3. Results

3.1. Nanoemulsion microfluidization and optical sensing

In total, $n = 11$ nanoemulsions were manufactured using consistent settings and processing time. Of those nanoemulsions, $n = 9$ were considered successful and $n = 2$ processes failed due to technical issues. Of the analyzed sensor signals, nephelometry data was the most consistent indicator of the microfluidization process and concomitant particle size change. Fig. 1 shows the raw nephelometry sensor traces for each of the 9 successful (Fig. 1A) and 2 failed (Fig. 1B) processes. The red x-marks above the traces represent the time points of sampling for particle size analysis. The traces from the 9 successful processes were nearly superimposable after approximately the first minute. Conversely, the failed processes had traces that were dissimilar compared to the successful processes and amongst themselves. The technical failures represented by each failed trace included an airlock in the interac-

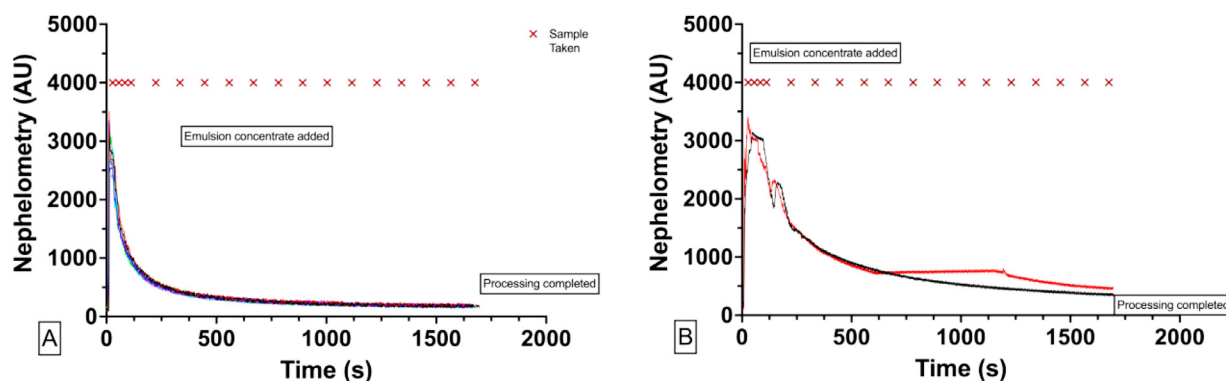


Fig. 1. Raw optical sensor nephelometry traces from 9 successful processes (A) and 2 failed processes (B). The maroon marks above the traces represent particle size analysis sampling times from the nanoemulsion.

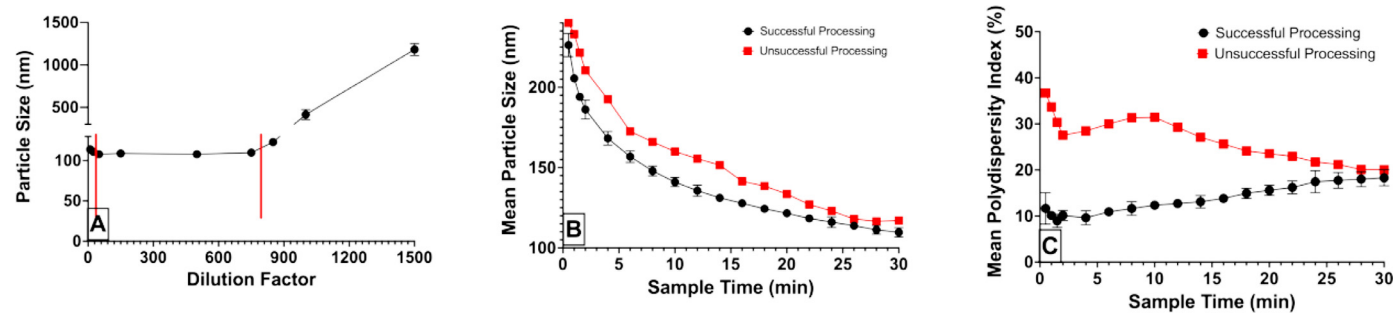


Fig. 2. A. The effect of dilution on particle size measurements in $n = 9$ nanoemulsions. B and C. The mean particle size and polydispersity index during the nanoemulsion processing for $n = 9$ successful experimental runs (black) and $n = 2$ unsuccessful runs.

tion chamber (black line, Fig. 1B) resulting in incomplete processing and inconsistent plunger stroke pressure due to a misaligned proximity switch (red line, Fig. 1B).

The sensor traces were nearly superimposable. There was an initial increase in signal due to the addition of the coarse nanoemulsion concentrate in each preparation. This was followed by a rapid decline in signal during the first discrete passes through the interaction chamber. Then a gradual approach to a signal plateau at the end of processing was observed.

3.2. Nanoemulsion particle sizing and stability

Fig. 2A shows the results of dilution experiments from $n = 3$ pilot nanoemulsions after full processing used to determine optimal settings for particle size analysis by DLS. As expected, lower dilutions (10 and 25X) resulted in overestimation of particle size due to particle-particle interactions. The particle size measurements were stable between 50–750X dilution (bracketed in red). At dilutions higher than 800X, particle size rapidly increased due to nanoemulsion destabilization.

Fig. 2B shows the mean particle size profile and Fig. 2C, the mean polydispersity index during the nanoemulsion processing for the 9 successful runs. The largest variation was observed at the early timepoints (0.5, 1 and 1.5 min) with variation within the measurement error for all

Other time points. The coefficient of variation for the measurements ranged from 0.6–4% across all timepoints. The mean polydispersity index was more variable and interestingly, increased over the time of processing to a plateau nearing 18% at about 26 min. For the 9 successful nanoemulsions, the mean particle size after processing was 110 ± 3 nm. For the 2 unsuccessful preparations, the mean particle size at the end of processing was 117 ± 7 nm and the polydispersity $\sim 20 \pm 0.5\%$. The particle size change was inconsistent in the unsuccessful preparations and the

Table 1

Longitudinal particle size analysis of 8 successful nanoemulsion preparations. Data are expressed as mean of all technical replicate means \pm SD for both particle size and polydispersity index (PDI). No particle size change or change in PDI was observed as size measurement was within measurement error at each timepoint.

Day	Diameter (nm)	SD (nm)	PDI (%)	SD (%)
0	111	4	18.6	1.9
4	107	5	17.7	1.2
14	109	8	18.5	0.7

polydispersity was significantly higher for the majority of processing. This likely accounted for the observed optical trace anomalies. Interestingly, on day 3–4, unlike the 9 successful preparations, the mean particle size of both unsuccessful preparations had grown to 153 ± 4 nm and 182 ± 6 nm, respectively, indicating the need for a consistent processing to maintain nanoemulsion stability.

Table 1 highlights the mean stability measurements for a sub-population (8 of 9) of the successful nanoemulsions examining DLS size and polydispersity measurements at day 3–5 and day 14 post manufacture compared to day 0. There was no significant change in particle size or polydispersity index over the 14 days at selected time points as all measurements were within the measurement error. In our prior works, where particle stability at 2 to 4 days translated to long term stability up to and exceeding 365 days in varied perfluorocarbon-based nanoemulsions, the measurements in Table 1 would be indicative of long-term nanoemulsion stability.

3.3. Nanoemulsion perfluorocarbon quantification by ATR-FTIR

Fig. 3 shows representative spectra of the two standards (nanoemulsion aqueous phase solution and pure FC-43) and a nanoemulsion concentrate and final diluted product. The region

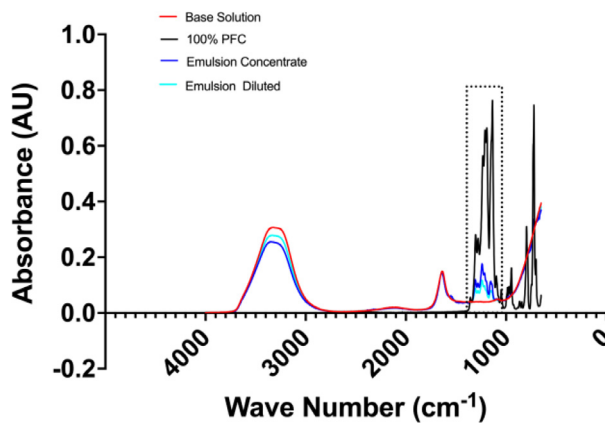


Fig. 3. Representative ATR-FTIR spectra for the base solution (red), pure FC-43 (black), nanoemulsion concentrate (dark blue) and final diluted nanoemulsion (light blue).

bounded by the dashed line represents the area utilized for AUC calculations and FC-43 quantification.

The mean perfluorocarbon content in the nanoemulsion concentrates ($n = 9$) was $17.4 \pm 0.7\%$, slightly higher than the expected 16.67% from the recipe. The mean perfluorocarbon concentration after final dilution ($n = 9$) was $10.8 \pm 0.5\%$, again, higher than the expected 10% v/v. In measurements of the concentrate and the final diluted nanoemulsion, the coefficients of variation were 5.0 and 4.1 %, respectively, amongst the $n = 9$ preparations.

3.4. Derivation of particle size algorithm from nephelometry data

Fig. 4A shows the plot of the mean nephelometry signal (AU) versus the mean measured particle sizes from the $n = 9$ nanoemulsions during processing. Least squares logistic curve fitting (natural log) was performed under the hypothesis that as particle size decreased and the nanoemulsions became more transparent, the signal would approach a plateau (minimal nephelometry). The goodness of fit coefficient of determination (R^2) was 0.99, indicating a significant relationship between the nephelometry signal and the measured particle sizes of the nanoemulsions during all phases of the processing.

The best-fit equation was then utilized to generate predicted particle sizes based on the corresponding nephelometry values from all processing time points of the $n = 9$ nanoemulsions. **Fig. 4B** displays the plot of measured particle sizes versus corresponding predicted particle sizes. The Deming regression of the data sets, which finds the best fit in x and y thereby accounting for errors in observations on both axes, is represented by the solid black line. Normality tests confirmed that the data was not normally distributed and the non-parametric (non-Gaussian) Spearman correlation analysis was performed on the data points. The Spearman R was 0.98 with a two-tailed p-value $< 1 \times 10^{-15}$ indicating that the predictive ability of the logistic algorithm relating nephelometry to measure particle size was highly significant.

Fig. 4C shows the Bland-Altman plot of the data sets, as the measured and predicted particle sizes were expected to quantify the same construct. Of the 183 points measured, 9 points fell outside of the limits of agreement (< 5%), indicated by red dots, meeting the *a priori* acceptable designated limits of agreement. The mean difference between the two measures was -0.09125 and there was no statistical indication of a systematic fixed bias, heteroscedasticity or other proportional or inconsistent variability. This was confirmed by the single sample t-test p-value of 0.367. Based on these results and the strong correlation between the sample measurements, the regression algorithm of the nephelometry

signal could be used to determine particle size in real-time during processing by adding code into the Arduino program data output supplied to the macOS Terminal Emulator.

3.5. Effective oxygen diffusivity and mass transfer enhancement in PFC nanoemulsions

The purpose of the measurements of effective oxygen diffusivity was to quantify the mass transfer enhancement afforded by the perfluorocarbon nanoemulsions relative to control encapsulation solutions. The measured increases in effective diffusivity and published increases in oxygen solubility resulted in a nearly four-fold predicted increase in oxygen mass transfer in capsules containing perfluorocarbon nanoemulsions relative to control solutions. **Fig. 5** shows the individual control and nanoemulsion diffusive permeability coefficients ($n = 5$) determined from the oxygen diffusion measurements.

The mean diffusive permeability coefficient for all 8 nanoemulsions was $2.22 \times 10^{-13} \pm 4.45 \times 10^{-14}$ mol/cm/mmHg/s while the mean value for the control solution was $4.51 \times 10^{-14} \pm 5.47 \times 10^{-15}$. The coefficient of variation between the nanoemulsion values was 20%.

3.6. Baseline oxygen consumption measurements and FEM

The purpose of oxygen consumption measurements and finite element modeling was to predict the oxygen profiles experienced by encapsulated cell aggregates under standard loading densities and varied oxygen consumption rates within the range characteristic of the cell clusters utilized. The mean oxygen consumption rate from $n = 4$ experimental replicates ($n = 4$ technical replicates per experiment) was $1.6 \times 10^{-2} \pm 7.4 \times 10^{-3}$ mol/m³/s. A parametric sweep around the mean \pm several SD was utilized in FEM to determine changes in tissue oxygen profiles and anoxic tissue percentages related to oxygen consumption rate. **Fig. 6** shows the results of the FEM relationship between anoxic tissue volume and oxygen consumption rate in the two polymer capsule configurations.

At OCRs below 0.008 mol/m³, there was no evidence of anoxic tissue in either group. With initial increases in oxygen consumption rate, the anoxic tissue volume increased in the control group at a faster rate than within the perfluorocarbon capsule group. At all increased consumption rates, the anoxic tissue volume was greater in the control group. At the highest rates (0.03–0.04 mol/m³/s) the anoxic tissue volume in the perfluorocarbon group began to approach the level in the control group due to the decrease in viable oxygen consuming volume in the control group (OCR = 0 in tissue partial pressures of oxygen less than 0.1 mmHg).

3.7. MIN-6 cluster encapsulation and polymer characterization

Fig. 7 shows mean flow (A) and viscosity (B) curves for 1.6% UP-MVG alginate made with PBS -/- (red lines) and perfluorocarbon nanoemulsion, respectively, from $n = 3$ encapsulations. Both types of alginate solution behaved similarly with no significant differences at any shear rate. As expected, the curves were characteristic of the shear thinning behavior associated with sodium alginate and other hydrogels.

The mean osmolarity of the control and perfluorocarbon alginate solutions done by freezing point osmometry ($n = 3$ solutions per group, 3 technical replicate measurements per solution) was 306 ± 3 mOsm and 308 ± 5 mOsm, respectively. The osmolarity was not significantly different. Importantly, PBS -/- was chosen as the physiological solvent for both alginate solutions because of its characteristic osmolarity of ~280–320 mOsm, with the addition of sodium alginate, there is an increased oncotic pressure of about 30 mOsm bringing the final osmolarity to the observed values of

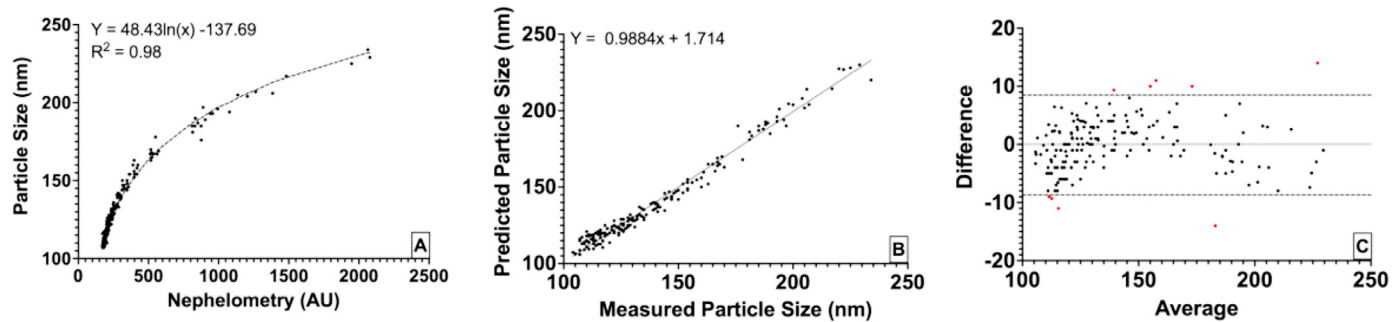


Fig. 4. Mean nephelometry signal (AU) versus mean measured particle sizes during processing of $n = 9$ nanoemulsions (A). Measured particle size versus predicted particle (B). Predicted particle size (y-axis) versus measured particle size (x-axis) in nm for all time points of processing from $n = 9$ nanoemulsions. Predicted particle size was calculated using logistic regression fit of mean nephelometry values versus measured particle size and then applying individual nephelometry values to equation. Bland-Altman analysis of measured versus predicted particle size (C).

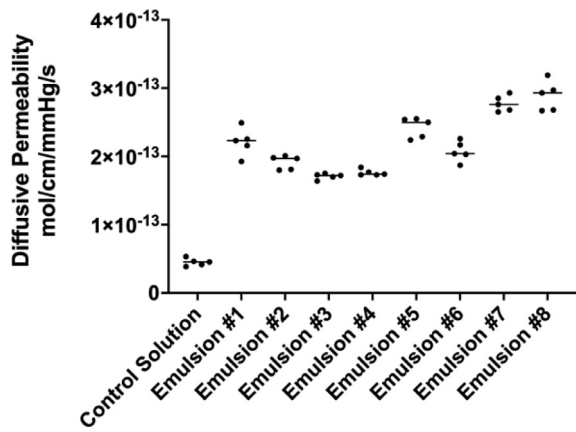


Fig. 5. Calculated diffusive permeability coefficients for $n = 8$ nanoemulsion preparations and control base solution. Coefficients were calculated using published literature Bunsen solubility coefficients and measured effective diffusivity. By one way ANOVA, all of the nanoemulsions exhibited significantly higher oxygen diffusive permeability than the control solution ($p < 1 \times 10^{-12}$).

~310–350 mOsm. The use of buffers, such as Hanks Balanced Salt Solution with an osmolarity ~300 mOsm, can cause an untoward increase in capsule osmolarity and put stress on the encapsulated cells.

Fig. 8 shows representative control alginate (A) and perfluorocarbon nanoemulsion supplemented alginate (B) capsules. The mean capsule diameters for the control and perfluorocarbon nanoemulsion capsules were $926 \pm 37 \mu\text{m}$ and $922 \pm 71 \mu\text{m}$, respectively.

The corresponding volumes were $418 \pm 49 \text{ nL}$ and $418 \pm 95 \text{ nL}$, respectively. The consistency in capsule size and material viscosity between the two groups insured that no observed differences in viability were due to material or reduced diffusion differences.

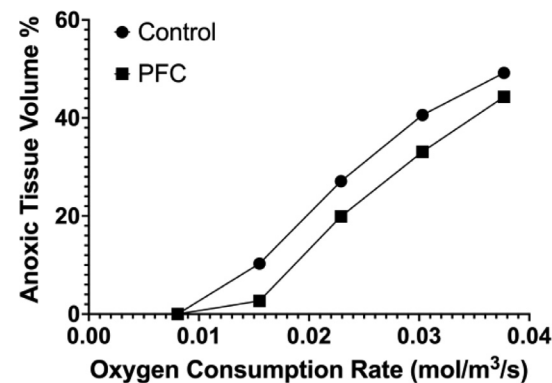


Fig. 6. Finite element modeling estimates of anoxic tissue volume percentages in control (black circles) and perfluorocarbon nanoemulsion (black squares) capsules containing MIN-6 clusters.

3.8. Encapsulated MIN-6 cluster viability and tissue hypoxia imaging

Fig. 9 Left shows the viability results at day 2 and day 4 post-encapsulation relative to the unencapsulated baseline viability values for both the control and perfluorocarbon nanoemulsion configurations. At both timepoints, the viability in the perfluorocarbon capsules was significantly higher than both the baseline values ($p = 1.7 \times 10^{-3}$ and $p = 0.02$ vs day 2 nanoemulsion and day 4 nanoemulsion, respectively) and the corresponding control capsules ($p = 8.0 \times 10^{-5}$ and 1.2×10^{-3} for day 2 and day 4, respectively). In fact, the viability in the PFC capsules was 4 to 5-fold that of the control capsules at both time points. To insure that this observed effect was not due to issues with dye penetration into the capsules, lysis controls were utilized in each capsule configuration (far right data set). The lysis values were not statistically different between the control and PFC groups and were plotted together, in-

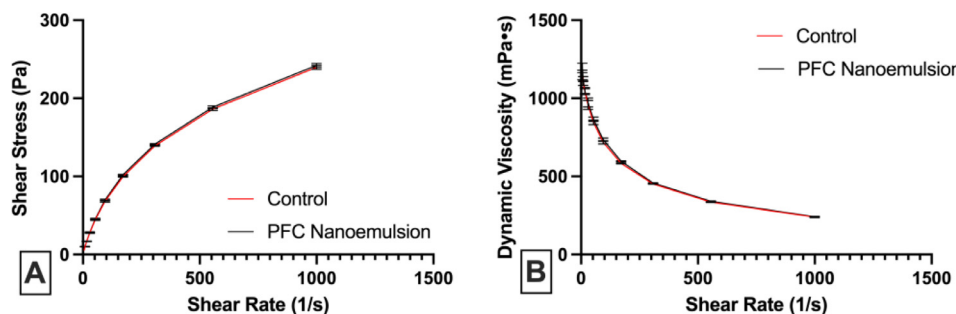


Fig. 7. Flow (A) and viscosity (B) curves for control 1.6% UP-MVG alginate solutions made with PBS -/- (red lines) and perfluorocarbon nanoemulsions (black lines).

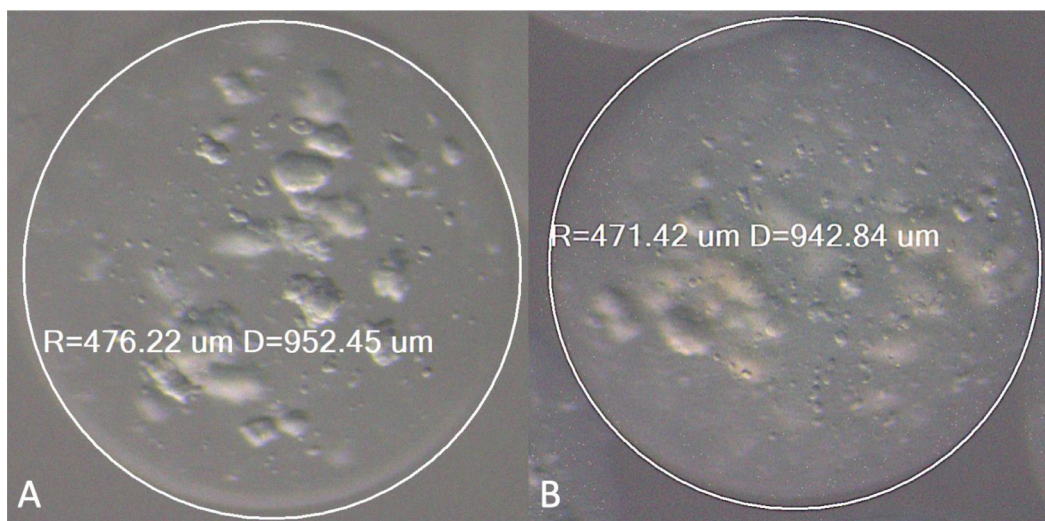


Fig. 8. Representative control alginate (A) and perfluorocarbon supplemented alginate (B) capsules containing MIN-6 clusters.

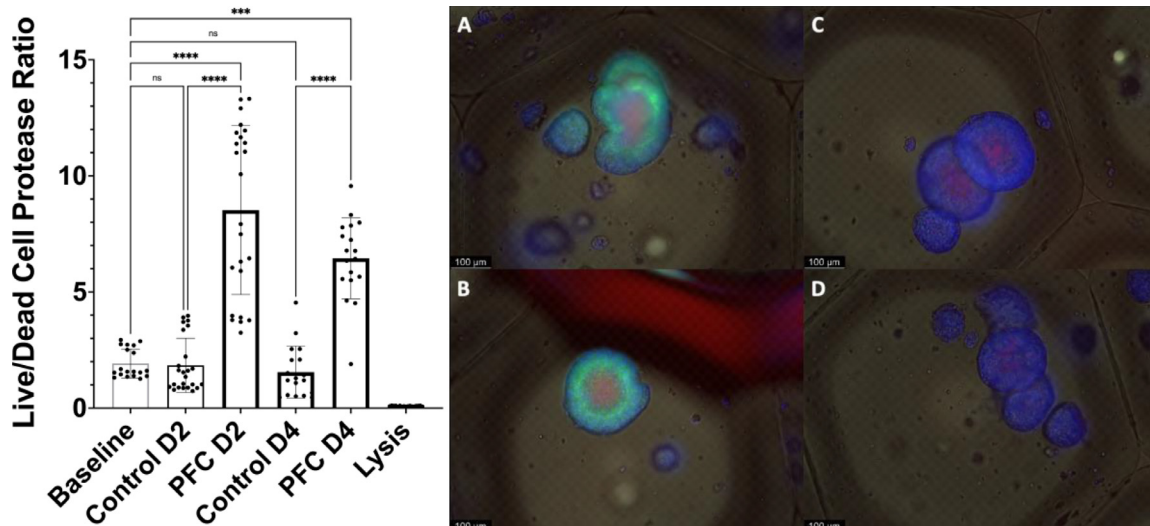


Fig. 9. Left Results of MultiTox Fluor cytotoxicity assay at D2 and D4 post-encapsulation relative to unencapsulated baseline values and control versus perfluorocarbon at each timepoint. Viability was significantly higher in the perfluorocarbon containing group relative to control and to baseline values and was not effected by issues of dye permeability, as evidenced by lysis controls. Viability in the day 2 and day 4 nanoemulsion group was significantly higher by Kruskal-Wallis non-parametric analysis than the control ($p = 8.0 \times 10^{-5}$ and 1.2×10^{-3} for day 2 and day 4, respectively) and the baseline unencapsulated clusters ($p = 1.7 \times 10^{-3}$ and $p = 0.02$ vs day 2 nanoemulsion and day 4 nanoemulsion, respectively). Conversely, the viability in the control group at day 2 and day 4 was not significantly different from the baseline values. Fig. 9 Right Representative imaging of hypoxia (green), dead cell (red) and nuclei (blue) in encapsulated MIN-6 clusters within control 1.6% UP-MVG alginate capsules (A and B) and in 1.6% UP-MVG alginate capsules made with 10% v/v perfluorocarbon/albumin nanoemulsion (C and D).

dicating that the dye was able to equivalently reach the clusters in both configurations.

Fig. 9 Right shows representative fluorescence photomicrographs of control (A and B) and perfluorocarbon nanoemulsion (C and D) containing capsules. The images were selected to have equivalent cluster numbers and positioning within the capsules. In the control images, a pO_2 of less than 38–40 mmHg was evident throughout the entire viable tissue and the core regions were necrotic as evidenced by the large area of bright dead cell staining ($> 100 \mu\text{m}$). The hypoxic signal in the surface regions was strong indicating a pO_2 well below the cutoff for fluorescence of $\sim 38 \text{ mmHg}$ (5%). Conversely, in the PFC nanoemulsion containing capsules there was no evidence of hypoxia and more diffuse dead cell staining with reduced regions of central necrosis. This was in line with the observed viability results using the MultiTox Fluor cytotoxicity assay.

Interestingly, the lack of hypoxia staining, indicating $pO_2 > 38$ –40 mmHg, in the nanoemulsion containing capsules was not in

agreement with the finite element models suggesting that the models of our group and others may underestimate the intracapsular oxygen profiles/levels with the addition of perfluorocarbons for enhanced oxygen transfer.

4. Discussion

The use of optical sensors in the fluid path during nanoemulsion processing could be a valuable tool in the production of new drug formulations and reformulations of existing drugs. The ability to track processing in real-time can be used, as in this work, to guide the duration of homogenization and as a quantitative criteria for process quality assurance. Beyond optical sensors, our development is focused on an array of other process sensors, such as temperature, pressure and audio data to derive quantitative targets/guidelines for successful processing of any drug-laden nanoemulsion formulation. What we learned in this initial study was that the quantitative values generated by the sensor, while im-

portant, were less informative than the actual longitudinal curves generated during the processing. All of this processing information could be supplied by an array of modular sensors feeding their signals into a software platform where it could be charted in real time. The long term goal would be to assemble process data for various formulations and generate a database for use in future applications.

Perfluorocarbon nanoemulsions have been investigated for many years as oxygen carrying therapeutics in a variety of applications including but not limited to blood replacement, imaging and cellular encapsulation. Traditionally, these nanoemulsions have been fabricated with a variety of intermediate phases/surfactants either from the lipid or polyethylene glycol (PEG) di-block copolymer family [10,19,20,24,25,29,47–50]. The use of these intermediate phases offers reasonable nanoemulsion stability and the ability to achieve sub-200 nm particle sizes but comes with the counterintuitive property of impaired oxygen transfer associated with PEG compounds [51,52]. We have also noted cytotoxicity related to PEG-based stabilizers [25]. As well, lipid emulsifiers can have the undesirable characteristic of oxidation byproducts that are toxic to cells [53–55].

Albumin, on the other hand, is a native serum protein that makes up between 3.4–5.4 w% of the blood. It is 50% of the blood protein content and accounts for 75–80% of the colloid oncotic pressure in the blood. This maintenance of oncotic pressure is critical in preventing fluid leakage into tissue (edema). Therefore, it is often used as a plasma expander in critical care situations. Albumin also acts as an important transporter for vitamins, hormones and enzymes throughout the body. As an intermediate phase for oxygen carrying nanoemulsions utilized in critical care, albumin is a desirable emulsifying agent due to its plasma expanding properties and lack of immunogenicity and cytotoxicity. Investigated applications for perfluorocarbon nanoemulsions include artificial blood substitutes, organ perfusion solutions and as carriers for the intravenous reformulation of anesthetics [10,19,20,25,47–50,56]. All of these have typically utilized lipid and alternate surfactants or combinations of emulsifying agents. A simplification of these recipes with a single, native blood protein could eliminate previously observed immune reactions and has the potential for utilization in numerous critical care applications including battlefield medicine, organ preservation and emergency medicine/critical cardiac care, to name a few.

One critical property in the biocompatibility of nanoemulsions is the requirement of sub-200 nm particle size, both for the ease of filter sterilization and lack of immunogenicity associated with this size range. To date, many perfluorocarbon nanoemulsion formulations have failed to achieve this particle size and stability and, as a result, have induced adverse physiological responses such as histamine flush and complement activation [30,57]. Our prior work demonstrated that the choice of perfluorocarbon has the greatest influence on particle size and stability independent of the PEG-based surfactant utilized as a stabilizing agent [25]. This property did not change when we introduced halogenated ethers into the perfluorocarbon phase of the nanoemulsions [10]. Therefore, we hypothesized that the introduction of albumin as the emulsifying agent would allow us to manufacture similar sub-120 nm nanoemulsions with the desirable properties of a single, non-immunogenic emulsifying agent.

5. Conclusions

In this work, we describe two advances in the field of nanoemulsion technologies. The first, the development of an optical sensor array to longitudinally monitor nanoemulsion production. This is critical in the field of drug development as problems during processing can result in cost overruns and sub-optimal

product. Additionally, the acquisition of optical data during processing allows for the rapid development of standardized manufacturing protocols as variables such as pressure, temperature and time of emulsification can be quantified by changes in optical signal and therefore, particle size/polydispersity. To test the efficacy of this system, we utilized the optical sensor array to manufacture sub-120 nm perfluorocarbon nanoemulsions with an intermediate phase comprised solely of 5% w/v bovine serum albumin. The oxygen-carrying ability of these nanoemulsions and their effect on cell viability was tested using the encapsulation of 3D endocrine clusters (MIN-6) cells.

The optical sensor array data demonstrated the function of the sensors in guiding consistent, reproducible nanoemulsion manufacture as demonstrated by the longitudinal plots of signal from both successful ($n = 9$) and unsuccessful ($n = 2$) processing runs. The data collected during the unsuccessful processing runs also demonstrated the utility of the array in detecting manufacturing issues. In the context of drug delivery, where a contract large volume processing run can cost in excess of 1 million dollars, the ability to detect issues before process completion could reduce cost overruns passed on to consumers. Importantly, the sensor data correlated well and was in significant agreement (predicted vs measured) with the gold-standard of random particle size measurements indicating that a processing algorithm could be implemented in the data stream supplying real-time particle size measurements.

The perfluorocarbon nanoemulsions manufactured using 5% w/v albumin as an intermediate phase were consistently sub-150 nm and easily sterile filtered and incorporated into 1.6% UP-MVG alginate solutions with no significant effect on the rheological properties. The use of the nanoemulsions as an oxygen-carrying supplement for encapsulated 3D endocrine clusters significantly improved cell viability and eliminated tissue hypoxia, as evidenced by ratiometric cell protease activity and dead cell/hypoxia imaging. Interestingly, the level of tissue hypoxia exhibited by the perfluoro-nanoemulsion group was not in agreement with finite element models based on the coefficients utilized by ourselves and others. This suggests that these coefficients may underestimate the carrying-capacity of the nanoemulsions or that the cells have some transient compensatory behaviors to address hypoxia.

Further work will employ these sensor arrays in the manufacture of different nanoemulsion configurations to understand the utility of the device across a spectrum of compounds. It is our belief that they could be useful in the growing development of drug carrying nanoemulsions with diverse phases, based on the optical properties of the sensor array. The albumin stabilized nanoemulsions will also be further investigated as the single biocompatible emulsifying agent makes them an attractive choice for use in critical care environments. The dual action of oxygen carrying/drug delivery and hemodynamic stabilizer/plasma expander could extend the potential applications for these solutions.

Funding

Research reported in this manuscript was supported by funding from the National Institute of Diabetes and Digestive and Kidney Diseases of the National Institutes of Health under award number R01 DK116875 (CF) and the Diabetes Research Institute Foundation. The content is solely the responsibility of the authors and does not necessarily represent the official views of the National Institutes of Health.

Declaration of Competing Interest

Mr. Bardsley and Dr. Fraker are developing the sensor technologies for implementation in commercially available high pressure

homogenizers. As such, it is not possible to describe the components and assembly in detail but we are happy to discuss research use with investigators who wish to implement these devices in a collaboration.

Supplementary materials

Supplementary material associated with this article can be found, in the online version, at doi:[10.1016/j.actbio.2021.09.038](https://doi.org/10.1016/j.actbio.2021.09.038).

References

- [1] R. Zhang, Z. Zhang, D.J. McClements, Nanoemulsions: An emerging platform for increasing the efficacy of nutraceuticals in foods, *Colloids Surf. B Biointerfaces* 194 (2020) 111202.
- [2] J. Zhang, Z. Liu, C. Tao, X. Lin, M. Zhang, L. Zeng, X. Chen, H. Song, Cationic nanoemulsions with prolonged retention time as promising carriers for ophthalmic delivery of tacrolimus, *Eur. J. Pharm. Sci.* 144 (2020) 105229.
- [3] W. Xu, L. Huang, W. Jin, P. Ge, B.R. Shah, D. Zhu, J. Jing, Encapsulation and release behavior of curcumin based on nanoemulsions-filled alginate hydrogel beads, *Int. J. Biol. Macromol.* 134 (2019) 210–215.
- [4] R. Gupta, J. Shea, C. Scaife, A. Shurygina, N. Rapoport, Polymeric micelles and nanoemulsions as drug carriers: therapeutic efficacy, toxicity, and drug resistance, *J. Control Release* 212 (2015) 70–77.
- [5] K. Hormann, A. Zimmer, Drug delivery and drug targeting with parenteral lipid nanoemulsions - A review, *J. Control Release* 223 (2016) 85–98.
- [6] R.N. Lodaya, L.A. Brito, T.Y.H. Wu, A.T. Miller, G.R. Otten, M. Singh, D.T. O'Hagan, Stable nanoemulsions for the delivery of small molecule immune potentiators, *J. Pharm. Sci.* 107 (9) (2018) 2310–2314.
- [7] H.H. Tayeb, F. Sainsbury, Nanoemulsions in drug delivery: formulation to medical application, *Nanomedicine (Lond.)* 13 (19) (2018) 2507–2525.
- [8] M. Herneisey, L. Liu, E. Lambert, N. Schmitz, S. Loftus, J.M. Janjic, Development of Theranostic perfluorocarbon nanoemulsions as a model non-opioid pain nanomedicine using a quality by design (QbD) approach, *AAPS PharmSciTech.* 20 (2) (2019) 65.
- [9] Q. Zhong, B.C. Yoon, M. Aryal, J.B. Wang, T. Ilovitsh, M.A. Baikoghli, N. Hosseini-Nassab, A. Karthik, R.H. Cheng, K.W. Ferrara, R.D. Airan, Polymeric perfluorocarbon nanoemulsions are ultrasound-activated wireless drug infusion catheters, *Biomaterials* 206 (2019) 73–86.
- [10] B. Ashrafi, M.H. Tootoonchi, R. Bardsley, R.D. Molano, P. Ruiz, E.A. Pretto Jr., C.A. Fraker, Stable perfluorocarbon emulsions for the delivery of halogenated ether anesthetics, *Colloids Surf. B Biointerfaces* 172 (2018) 797–805.
- [11] L. Zhengguang, H. Jie, Z. Yong, C. Jiaoqiao, W. Xingqi, C. Xiaoqin, Study on the transdermal penetration mechanism of ibuprofen nanoemulsions, *Drug Dev. Ind. Pharm.* 45 (3) (2019) 465–473.
- [12] N. Zheng, Y. Gao, H. Ji, L. Wu, X. Qi, X. Liu, J. Tang, Vitamin E derivative-based multifunctional nanoemulsions for overcoming multidrug resistance in cancer, *J. Drug Target* 24 (7) (2016) 663–669.
- [13] D.A. Fernandes, D.D. Fernandes, Y. Li, Y. Wang, Z. Zhang, D. Rousseau, C.C. Grdinaru, M.C. Kolios, Synthesis of stable multifunctional perfluorocarbon nanoemulsions for cancer therapy and imaging, *Langmuir* 32 (42) (2016) 10870–10880.
- [14] P. Nirale, A. Paul, K.S. Yadav, Nanoemulsions for targeting the neurodegenerative diseases: Alzheimer's, Parkinson's and Prion's, *Life Sci.* 245 (2020) 117394.
- [15] A. Said Suliman, R. Tom, K. Palmer, I. Tolaymat, H.M. Younes, B. Arafat, A.M.A. Elhissi, M. Najlah, Development, characterization and stability evaluation of ciprofloxacin-loaded parenteral nutrition nanoemulsions, *Pharm. Dev. Technol.* 25 (5) (2020) 579–587.
- [16] L.C. Clark Jr., E.P. Wessel, M.L. Miller, S. Kaplan, Ring versus straight chain perfluorocarbon emulsions for perfusion media, *Microvasc. Res.* 8 (3) (1974) 320–340.
- [17] C.A. Hall, Perfluorocarbon emulsions in the perfusion of canine organs, *Fed. Proc.* 34 (6) (1975) 1513–1514.
- [18] R.L. Goodman, R.E. Moore, M.E. Davis, D. Stokes, J.M. Yuhas, Perfluorocarbon emulsions in cancer therapy: preliminary observations on presently available formulations, *Int. J. Radiat. Oncol. Phys.* 10 (8) (1984) 1421–1424.
- [19] N.S. Faithfull, P.J. Salt, J. Klein, H.T. van der Zee, H. Soini, W. Erdmann, Gas exchange during peritoneal perfusion with perfluorocarbon emulsions, *Adv. Exp. Med. Biol.* 191 (1985) 463–472.
- [20] B.D. Spiess, Perfluorocarbon emulsions: one approach to intravenous artificial respiratory gas transport, *Int. Anesthesiol. Clin.* 33 (1) (1995) 103–113.
- [21] J. Wolber, I.J. Rowland, M.O. Leach, A. Bifone, Perfluorocarbon emulsions as intravenous delivery media for hyperpolarized xenon, *Magn. Reson. Med.* 41 (3) (1999) 442–449.
- [22] M.L. Fabiilli, J.A. Lee, O.D. Kripfgans, P.L. Carson, J.B. Fowlkes, Delivery of water-soluble drugs using acoustically triggered perfluorocarbon double emulsions, *Pharm. Res.* 27 (12) (2010) 2753–2765.
- [23] D.S. Li, S. Schneewind, M. Bruce, Z. Khaing, M. O'Donnell, L. Pozzo, Spontaneous nucleation of stable perfluorocarbon emulsions for ultrasound contrast agents, *Nano Lett.* 19 (1) (2019) 173–181.
- [24] C.A. Fraker, A.J. Mendez, C.L. Stabler, Complementary methods for the determination of dissolved oxygen content in perfluorocarbon emulsions and other solutions, *J. Phys. Chem. B* 115 (35) (2011) 10547–10552.
- [25] C.A. Fraker, A.J. Mendez, L. Inverardi, C. Ricordi, C.L. Stabler, Optimization of perfluoro nano-scale emulsions: the importance of particle size for enhanced oxygen transfer in biomedical applications, *Colloids Surf. B Biointerfaces* 98 (2012) 26–35.
- [26] M. Tootoonchi, R. Bardsley, T. Panagiotou, R.J. Fisher, E.A. Pretto, C. Fraker, Rapid quantification of isoflurane in anesthetic nanoemulsions using Attenuated total reflectance fourier transform infrared spectroscopy (ATR-FTIR), *Vib. Spectrosc. Accept. Publ.* (2020).
- [27] R.A. Johnson, K.T. Simmons, J.P. Fast, C.A. Schroeder, R.A. Pearce, R.M. Albrecht, S. Mecozzi, Histamine release associated with intravenous delivery of a fluorocarbon-based sevoflurane emulsion in canines, *J. Pharm. Sci.* 100 (7) (2011) 2685–2692.
- [28] J.P. Jee, M.C. Parlato, M.G. Perkins, S. Mecozzi, R.A. Pearce, Exceptionally stable fluorous emulsions for the intravenous delivery of volatile general anesthetics, *Anesthesiology* 116 (3) (2012) 580–585.
- [29] J.P. Fast, M.G. Perkins, R.A. Pearce, S. Mecozzi, Fluoropolymer-based emulsions for the intravenous delivery of sevoflurane, *Anesthesiology* 109 (4) (2008) 651–656.
- [30] R.J. Noveck, E.J. Shannon, P.T. Leese, J.S. Shorr, K.E. Flaim, P.E. Keipert, C.M. Woods, Randomized safety studies of intravenous perflubron emulsion. II. Effects on immune function in healthy volunteers, *Anesth. Analg.* 91 (4) (2000) 812–822.
- [31] P.T. Leese, R.J. Noveck, J.S. Shorr, C.M. Woods, K.E. Flaim, P.E. Keipert, Randomized safety studies of intravenous perflubron emulsion. I. Effects on coagulation function in healthy volunteers, *Anesth. Analg.* 91 (4) (2000) 804–811.
- [32] C. Assenheimer, L.J. Machado, B. Glasse, U. Fritsching, R. Guardani, Use of a spectroscopic sensor to monitor droplet size distribution in emulsions using neural networks, *Can. J. Chem. Eng.* 92 (2014) 318.
- [33] A. Wrobeln, J. Laudien, C. Gross-Heitfeld, J. Linders, C. Mayer, B. Wilde, T. Knoll, D. Naglav, M. Kirsch, K.B. Ferenz, Albumin-derived perfluorocarbon-based artificial oxygen carriers: a physico-chemical characterization and first *in vivo* evaluation of biocompatibility, *Eur. J. Pharm. Biopharm.* 115 (2017) 52–64.
- [34] A. Wrobeln, K.D. Schluter, J. Linders, M. Zahres, C. Mayer, M. Kirsch, K.B. Ferenz, Functionality of albumin-derived perfluorocarbon-based artificial oxygen carriers in the Langendorff-heart (dagger), *Artif. Cells Nanomed. Biotechnol.* 45 (4) (2017) 723–730.
- [35] Z. Zhou, B. Zhang, H. Wang, A. Yuan, Y. Hu, J. Wu, Two-stage oxygen delivery for enhanced radiotherapy by perfluorocarbon nanoparticles, *Theranostics* 8 (18) (2018) 4898–4911.
- [36] H. Ren, J. Liu, F. Su, S. Ge, A. Yuan, W. Dai, J. Wu, Y. Hu, Relighting photosensitizers by synergistic integration of albumin and perfluorocarbon for enhanced photodynamic therapy, *ACS Appl. Mater. Interfaces* 9 (4) (2017) 3463–3473.
- [37] T. Porter, D. Kricsfeld, S. Cheatham, S. Li, Effect of blood and microbubble oxygen and nitrogen content on perfluorocarbon-filled dextrose albumin microbubble size and efficacy: *in vitro* and *in vivo* studies, *J. Am. Soc. Echocardiogr.* 11 (5) (1998) 421–425.
- [38] J. Crank, *The Mathematics of Diffusion*, Oxford University Press, 1956.
- [39] A.S. Johnson, E. O'Sullivan, L.N. D'Aoust, A. Omer, S. Bonner-Weir, R.J. Fisher, G.C. Weir, C.K. Colton, Quantitative assessment of islets of Langerhans encapsulated in alginate, *Tissue Eng. Part C Methods* 17 (4) (2011) 435–449.
- [40] C.A. Fraker, S. Cechin, S. Alvarez-Cubela, F. Echeverri, A. Bernal, R. Poo, C. Ricordi, L. Inverardi, J. Dominguez-Bendala, A physiological pattern of oxygenation using perfluorocarbon-based culture devices maximizes pancreatic islet viability and enhances beta-cell function, *Cell Transplant.* 22 (9) (2013) 1723–1733.
- [41] K.K. Papas, M.D. Bellin, D.E. Sutherland, T.M. Suszynski, J.P. Kitzmann, E.S. Avgoustiniatos, A.C. Guessner, K.R. Mueller, G.J. Beilman, A.N. Balamurugan, G. Loganathan, C.K. Colton, M. Koulmard, G.C. Weir, J.J. Wilhelm, D. Qian, J.C. Niland, B.J. Hering, Islet oxygen consumption rate (OCR) dose predicts insulin independence in clinical islet autotransplantation, *PLoS One* 10 (8) (2015) e0134428.
- [42] K.K. Papas, C.K. Colton, R.A. Nelson, P.R. Rozak, E.S. Avgoustiniatos, W.E. Scott, G.M. Wildey 3rd, A. Pisania, G.C. Weir, B.J. Hering, Human islet oxygen consumption rate and DNA measurements predict diabetes reversal in nude mice, *Am. J. Transplant.* 7 (3) (2007) 707–713.
- [43] K.K. Papas, A. Pisania, H. Wu, G.C. Weir, C.K. Colton, A stirred microchamber for oxygen consumption rate measurements with pancreatic islets, *Biotechnol. Bioeng.* 98 (5) (2007) 1071–1082.
- [44] S. Cechin, S. Alvarez-Cubela, J.A. Giraldo, R.D. Molano, S. Villate, C. Ricordi, A. Pileggi, L. Inverardi, C.A. Fraker, J. Dominguez-Bendala, Influence of *in vitro* and *in vivo* oxygen modulation on beta cell differentiation from human embryonic stem cells, *Stem Cells Transl. Med.* 3 (3) (2014) 277–289.
- [45] C.A. Fraker, S. Alvarez, P. Papadopoulos, J. Giraldo, W. Gu, C. Ricordi, L. Inverardi, J. Dominguez-Bendala, Enhanced oxygenation promotes beta-cell differentiation *in vitro*, *Stem Cells* 25 (12) (2007) 3155–3164.
- [46] H.M. Tse, G. Gardner, J. Dominguez-Bendala, C.A. Fraker, The Importance of proper oxygenation in 3D culture, *Front. Bioeng. Biotechnol.* 9 (2021) 634403.
- [47] M.G. Freire, A.M. Dias, M.A. Coelho, J.A. Coutinho, I.M. Marrucho, Aging mechanisms of perfluorocarbon emulsions using image analysis, *J. Colloid Interface Sci.* 286 (1) (2005) 224–232.
- [48] E. Maillard, M.T. Juszczak, A. Langlois, C. Kleiss, M.C. Sencier, W. Bietiger, M. Sanchez-Dominguez, M.P. Kraft, P.R. Johnson, M. Pinget, S. Sigrist, Perfluorocarbon emulsions prevent hypoxia of pancreatic beta-cells, *Cell Transplant.* 21 (4) (2012) 657–669.

- [49] A.J. McGoron, R. Pratt, J. Zhang, Y. Shiferaw, S. Thomas, R. Millard, Perfluorocarbon distribution to liver, lung and spleen of emulsions of perfluorotributylamine (FTBA) in pigs and rats and perfluoroctyl bromide (PFOB) in rats and dogs by ^{19}F NMR spectroscopy, *Artif. Cells Blood. Substit. Immobil. Biotechnol.* 22 (4) (1994) 1243–1250.
- [50] D.R. Spahn, P.E. Keipert, An overview of two human trials of perfluorocarbon emulsions in noncardiac surgery, *Shock* 52 (2019) 116–118 1S Suppl 1.
- [51] C. Ho, Oxygen diffusion coefficients in polymeric solutions, *Chem. Eng. Sci.* 41 (3) (1986) 579–589.
- [52] J. Mexal, Oxygen availability in polyethylene glycol solutions and its implications in plant-water relations, *Plant Physiol.* 55 (1975) 20–24.
- [53] D.J. McClements, B. Ozturk, Utilization of nanotechnology to improve the handling, storage and biocompatibility of bioactive lipids in food applications, *Foods* 10 (2) (2021).
- [54] Q. Liu, H. Huang, H. Chen, J. Lin, Q. Wang, Food-grade nanoemulsions: preparation, stability and application in encapsulation of bioactive compounds, *Molecules* 24 (23) (2019).
- [55] S.J. Choi, D.J. McClements, Nanoemulsions as delivery systems for lipophilic nutraceuticals: strategies for improving their formulation, stability, functionality and bioavailability, *Food Sci. Biotechnol.* 29 (2) (2020) 149–168.
- [56] N. Shah, A. Mehra, Modeling of oxygen uptake in perfluorocarbon emulsions. Some comparisons with uptake by blood, *ASAO J.* 42 (3) (1996) 181–189.
- [57] P.E. Keipert, S. Otto, S.F. Flaim, J.G. Weers, E.A. Schutt, T.J. Pelura, D.H. Klein, T.L. Yaksh, Influence of perflubron emulsion particle size on blood half-life and febrile response in rats, *Artif. Cells Blood. Substit. Immobil. Biotechnol.* 22 (4) (1994) 1169–1174.